Spatially distributed characterization of hyporheic solute transport during baseflow recession in a headwater mountain stream using electrical geophysical imaging

Adam S. Ward [a,b,*], Michael N. Gooseff [c], Michael Fitzgerald [d], Thomas J. Voltz [e], Kamini Singha [f]

[a] School of Public and Environmental Affairs, Indiana University, Bloomington, IN 47405, USA
[b] Department of Earth & Environmental Sciences, The University of Iowa, Iowa City, IA 52242, USA
[c] Department of Civil and Environmental Engineering, Colorado State University, Fort Collins, CO 80523, USA
[d] National Ecological Observatory Network, Boulder, CO 80301, USA
[e] University of Applied Sciences, Faculty of Civil Engineering/Architecture, Division of Water Sciences, Friedrich-List-Platz 1, 01069 Dresden, Germany
[f] Hydrologic Science and Engineering, Colorado School of Mines, Golden, CO 80402, USA

ARTICLE INFO

SUMMARY

The transport of solutes along hyporheic flowpaths is recognized as central to numerous biogeochemical cycles, yet our understanding of how this transport changes with baseflow recession, particularly in a spatially distributed manner, is limited. We conducted four steady-state solute tracer injections and collected electrical resistivity data to characterize hyporheic transport during seasonal baseflow recession in the H.J. Andrews Experimental Forest (Oregon, USA). We used temporal moment analysis of pixels generated from inversion of electrical resistivity data to compress time-lapse data into descriptive statistics (mean arrival time, temporal variance, and temporal skewness) for each pixel. A spatial visualization of these temporal moments in the subsurface at each of five 2-D transects perpendicular to the stream was interpreted to inform transport processes. As baseflow recession progressed we found increasing first arrival times, persistence, mean arrival time, temporal variance, and coefficient of variation, and decreasing skewness. These trends suggest that changes in hydrologic forcing alter the relative influence of transport phenomena (e.g., advection vs. other transport processes such as dispersion) along flowpaths. Spatial coverage obtained from electrical resistivity images allowed for qualitative comparison of spatial patterns in temporal moments both at an individual cross-section as well as between cross sections. We found that geomorphologic controls (e.g., bedrock confinement vs. gravel wedge deposits) resulted in different distributions and metrics of hyporheic transport. Results of this study provide further evidence that hyporheic transport is highly variable both in space and through the baseflow recession period. Geophysical images differentiate advection-dominated flowpaths from those that are more affected by other transport processes (e.g., dispersion, mobile-immobile exchange).

© 2014 Elsevier B.V. All rights reserved.

1. Introduction and background

Despite a broad recognition of the ecological relevance of transport along hyporheic flowpaths (e.g., Boulton et al., 2010; Brunke and Gonser, 1997; Krause et al., 2011), relatively little is known about the distribution of hyporheic transport processes in the subsurface, and how this distribution changes with hydrological dynamics throughout a typical season. Recent field and numerical studies have demonstrated that travel time along hyporheic flowpaths is a primary control on associated biogeochemical cycling (Boano et al., 2010; Zarnetske et al., 2011). Indeed, studies by Battin (1999, 2000) demonstrate that hydrodynamics are a first-order control on ecological processes. Transport processes in the subsurface include advection, longitudinal dispersion along hyporheic flowpaths, and dispersion away from individual flowpaths (e.g., into less-mobile domains such as bound pore water). An improved ability to quantify spatiotemporally variable flow and transport patterns in the subsurface is necessary to predict ecologically relevant solute fluxes. Understanding the spatial distributions of temporal trends in hyporheic transport is a necessary step toward a process-based understanding of biogeochemical cycling in the subsurface and at the stream-reach scale.

* Corresponding author at: School of Public and Environmental Affairs, Indiana University, 430 MSB-II, Bloomington, IN 47405, USA. Tel.: +1 812 855 0635.
E-mail address: adamward@indiana.edu (A.S. Ward).

Because the boundary conditions controlling hyporheic exchange can be dynamic during baseflow recession (e.g., hydraulic gradients), we expect that transport processes in the subsurface will respond to dynamic forcing. At the reach scale, several studies have documented changes in transient storage (interpreted as evidence of hyporheic exchange changes) under different flow conditions. Numerical studies of pumping exchange found hyporheic flowpaths contract due to ambient gaining conditions (Boano et al., 2008; Cardenas and Wilson, 2007). Several field studies report contraction of hyporheic flowpaths during periods of increased groundwater discharge to streams (e.g., Harvey and Bencala, 1993; Storey et al., 2003; Williams, 1993; Wondzell and Swanson, 1996; Wroblicky et al., 1998), though findings of Ward et al. (2012a) challenge this conceptual model, demonstrating surprisingly little linkage between hydraulic gradients and hyporheic extent. Furthermore, Wondzell (2006) completed tracer studies in steep headwater catchments in the H.J. Andrews Experimental Forest under two different baseflow conditions (4.5 and 1 L s^{-1} in Watershed 1, 10 and 3 L s^{-1} in Watershed 3), finding that hyporheic extent, evaluated as tracer arrival in a monitoring well network, was not changed during baseflow recession. In a modeling study of one of the watersheds in their 2006 study, Wondzell et al. (2009) concluded that even complex physical models are insufficient to predict the movement of solute through the hyporheic zone. This shortcoming is attributed to the inability to identify unique model solutions and invalidate all other solutions, a problem which arises in part because spatially discrete measurements are used to infer up-gradient behavior along flowpaths. Indeed, hydrologic modeling efforts attempting to simulate a limited number of point measurements are plagued by problems of equifinality (e.g., Beven, 1993, 2006); an infinite number of realizations of the upstream system (e.g., the hydraulic conductivity field) can adequately produce the observed data. An ongoing debate about the usefulness of such models in predicting solute transport and fluxes at the scale of individual flowpaths continues in the literature (e.g., Bredehoeft and Konikow, 1993; Hassan, 2004; Konikow and Bredehoeft, 1992; Oreskes et al., 1994; Poeter, 2007; Wondzell et al., 2009).

Of particular interest is the characterization of process dynamics (i.e., characteristics that change through time and are inherently linked to the movement of fluids in the subsurface; Binley et al., 2010; Koch et al., 2009). Indeed, electrical resistivity (ER) imaging of solute tracers in hyporheic zones has been demonstrated in recent field trials (Cardenas and Markowski, 2011; Ward et al., 2010b, 2012a; Toran et al., 2012). For example, Ward et al. (2012a) used time-lapse ER images of saline tracer movement along hyporheic flowpaths as one tool to parameterize groundwater flow and transport models. Time-lapse ER has also been interpreted to inform subsurface structure and hyporheic extent from ER imaging during solute tracer studies (Ward et al., 2012a, 2013b). Such imaging provides high spatial and temporal resolution of solute transport in situ relative to piezometer sampling, and addresses some limitations of reach-scale studies that infer upstream behavior based on limited downstream observations in the surface stream.

The use of ER to characterize groundwater flow and transport processes is common (e.g., Singha and Gorelick, 2005, 2006; Koestel et al., 2009; Ward et al., 2013b) despite inherent uncertainty in inverted ER images (e.g., Slater et al., 2002; Day-Lewis et al., 2005, 2007). For example, inversion results are known to be smeared in space due to regularization and time due to data collection limitations (e.g., Singha and Gorelick, 2005; Doetsch et al., 2012). Promising areas of research that addresses these limitations include the inversion of the temporal moments of the electrical resistivity data rather than calculation of the temporal moments from a series of inversions (e.g., Pollock and Cirpka, 2008, 2010, 2012) and inversion schemes where hydrogeological constraints are included in the inverse problem (e.g., Jardani et al., 2013; Pidlisecky et al., 2011). Despite the limitations of ER, the utility of spatially extensive electrical resistivity imaging and the interpretation of resulting time series is still useful in characterization of heterogeneous transport processes in the shallow subsurface (Doetsch et al., 2012; Ward et al., 2010b, 2012a,b; Menichino et al., 2012; Toran et al., 2012).

Here, we capitalize on our imaging of processes through time to interpret solute transport behavior. Both qualitative and quantitative interpretations of individual pixel or finite-element behavior during saline tracer studies have proven useful. Individual pixels in a soil column experiment demonstrated characteristic trends of advection–dispersion behavior of tracer-labeled water moving through the column (Binley et al., 1996). In a 2-D laboratory experiment, Slater et al. (2000) interpreted pixel breakthrough curves to quantify first arrival times of tracer at individual pixels and recommended comparison of pore fluid with pixel values in ER images in future studies. In a 3-D laboratory study, Slater et al. (2002) demonstrated broad agreement between pore fluid conductivity and pixel resistivity. Their study demonstrates the value of a densely sampled, spatially continuous data set to observe greater complexity in transport processes than was possible with their flow and transport modeling alone. Kemna et al. (2002) compared ER image behavior with advection–dispersion modeling of groundwater flow and transport and were able to observe more complexity in flowpath behavior than was present in their numerical simulations of flow and transport. In a synthetic study, Ward et al. (2013b) used temporal moment analysis of pixels in inverted geophysical images as a calibration target for numerical models of hyporheic transport.

Here, we use time series analysis of several time series of 2-D electrical resistivity tomograms to characterize transport of solutes along hyporheic flowpaths in the subsurface. In a modeling study, Ward et al. (2010a) interpret the spatial distribution of temporal moments of solute time series and raw ER data (as opposed to reconstructed images) to infer transport processes in the subsurface. Results of their simulations identified areas where advection dominates other transport processes in the subsurface. They speculate that a similar analysis could be completed using time-lapse ER images collected during a field study. Temporal moment analysis has been used to describe the transport of solutes in the subsurface in several studies (e.g., Cirpka and Kitanidis, 2000; Day-Lewis and Singha, 2008; Singha et al., 2007) and has also been used to describe flow and transport in coupled stream-aquifer systems (e.g., Gupta and Cvetkovic, 2000; Schmid, 2003). Cirpka and Kitanidis (2000) interpret temporal moments of simulated tracer breakthrough curves at points in the subsurface to derive apparent subsurface solute velocity and dispersivity. In a numerical study of hyporheic exchange, Singha et al. (2008) calculate temporal moments based on reach-averaged concentrations within the stream and subsurface, and suggest moments calculated at a higher spatial resolution would be appropriate if variability is expected across a domain of interest.

The overarching objectives of this study are to (1) quantify the heterogeneity in subsurface transport, and (2) assess how solute transport processes in the hyporheic zone change during seasonal baseflow recession. We expect that changing boundary conditions during baseflow recession will change temporal trends in hyporheic solute transport in the subsurface (for example, later mean arrival times and increased temporal variance and skewness of solute tracer time series). To achieve this objective, we apply temporal moment analysis to ER images to provide spatially distributed solute transport information in the subsurface (i.e., to quantify where and when advection, dispersion and mobile-immobile exchange are occurring). This is an application of the spatially distributed analysis of numerical simulations by Ward et al. (2010a) to inverted images based on field data. We conducted

a series of replicate solute tracer studies (each 48 h long) and monitored tracer movement in the subsurface using electrical resistivity imaging in a small headwater stream. Spatially distributed characterization of temporal trends at each transect provides an assessment of flowpaths that are commonly beyond a tracer study's window of detection using in-stream tracer recovery or well data. We developed cumulative distribution functions (CDFs) describing temporal moments at each transect during each injection to compare transport behavior along flowpaths, and use a one-way ANOVA to identify significant differences along the stream and during different baseflow discharge conditions. Ultimately, understanding the distribution of transport processes provides a more complete assessment of transport than has been possible with reach-scale tracer studies and monitoring well networks.

2. Methods and background data

2.1. Site description

The field studies presented here were conducted in WS3 in the H.J. Andrews Experimental Forest, located in the Cascade Mountain Range in Oregon, USA (48°10′N, 122°15′W). The study watershed is a steep (hillslope gradients greater than 50% in the study reach), narrow (8.5 m wide valley bottom) catchment draining 101 ha and ranging in elevation from 497 to 1070 m above mean sea level. Shallow, highly porous loams are typically 1–2 m deep on the hillslopes (Dyrness, 1969). Saturated hydraulic conductivity in the valley bottom has been reported as 7×10^{-5} m s^{-1} (Kasahara and Wondzell, 2003), while Wondzell et al. (2009) report a geometric mean of 1.7×10^{-5} m s^{-1} for an adjacent headwater catchment. The substrate is highly permeable, comprised of relatively young organic material, coarse gravel, facilitating large preferential flowpaths along decaying trees that have fallen in the valley bottom. The upper portion of the reach (ER transects 1–3) is highly constrained by bedrock (Wondzell, 2006), with bedrock outcropping along the northeast valley wall and a small alluvial deposit along the opposite valley wall at ER transects 1–2. ER transect 3 is located at a bedrock "pinch-point" in the valley bottom, where both sides of the stream are confined by bedrock. The lower portion of the study reach (ER transects 4–5) has a flatter gradient and is wider, with no apparent bedrock outcropping. At transects 4–5, a large fallen tree and several boulders hold a wedge of alluvium in the valley bottom.

Studies were primarily focused on a short, second-order study reach with a down-stream gradient of 14% (Fig. 1A), including several pool, riffle, and step features. Kasahara and Wondzell (2003) report an average of 8.4 steps or riffles contributing an average of 54% of the elevation change along each 100 m reach. Flow is gauged at the outlet of WS3 at a permanent weir maintained by the U.S. Forest Service; flow ranged from 35 L s^{-1} early in the recession period to 4 L s^{-1} by the end of the study period (Fig. 1B).

Cross-sectional area of the stream is highly variable in space due to the stream morphology, and was not quantified during our field campaign. For discharge conditions of 35 L s^{-1}, Voltz et al. (2013) report a typical surface width of 4-m. Unpublished data from Voltz et al.'s study recorded stream centerline depth of 0.45-m at Transect 4 at the time of their survey. Assuming a rectangular channel of 4-m wide and 0.45-m deep, we estimate a stream cross-sectional area of 1.8 m^2 during Injection 1 of our study. Past studies at in WS3 report stream widths of 0.08, 1.30, and 1.80 m for discharges of 2.76, 3.23, and 4 L s^{-1} (Wondzell, 2006; Kasahara and Wondzell, 2003), which are comparable to our late-season studies. Argerich et al. (2011) report average width and depth of the stream as 2.04 m and 0.0485 m, respectively, for

discharge of 1.34 L s^{-1} in WS3. We did observed in-stream depth of 0.39-m at Transect 4 during Injection 4 of our study (Voltz, 2011). Assuming an average width of 1.8 m and depth of 0.39 m, we estimate an average cross-sectional area of 0.70 m^2 during Injection 4 in our study.

### 2.2. Solute tracer studies

We conducted four 48-h constant rate injections of sodium chloride (NaCl, assumed to behave as a conservative tracer) in the watershed, with injections at the same locations used by Wondzell (2006) (approximately 50 m upstream of the study reach; Ward et al., 2012a). Tracer was injected directly into the stream channel using a small pump, with each experiment designed to increase in-stream electrical conductivity (EC) by approximately 100 μS cm^{-1} above background conditions of approximately 40 μS cm^{-1}. For all measurements, EC was used as a surrogate for tracer concentration (after Gooseff and McGlynn, 2005; Payn et al., 2009; Ward et al., 2013a). All tracer studies began between 13:00 and 14:00 and lasted for 48 h. For each tracer study, the relative time elapsed is calculated form the time at which the injection began. Tracer presence in the surface water was recorded at the upstream end of the study reach using a temperature and EC probe manufactured by Campbell Scientific, Inc. (Logan, Utah, United States). EC measurements, collected in-stream, began prior to the injection and lasted for at least 120 h after the start of the injection.

The breakthrough curves for the four replicate tracer studies were logged at the upstream end of the study reach (Fig. 1C). Fluid conductivity immediately prior to the start of the injection was subtracted from each observation set to isolate the signal from the tracer. Plateau concentrations range from increases of approximately 60–120 μS cm^{-1} during the injection, due to differing in-stream and injection flow rates between injections. Injection flow rates were checked at intervals of 3–4 h to ensure a constant-rate injection into the stream. During tracer injection 1 the injection rate approximately doubled after about 39 h of injection (at approximately 03:00). This change was discovered at approximately 06:00 and the injection flow rate was reset to its initial rate.

Tracer arrival time at the study reach was fastest during the first injection, with first arrival occurring within minutes of the injection start time. Tracer arrival time increased with decreasing flow rate, ultimately reaching a time of approximately 20 min during the final, lowest flow rate injection. During all studies a gradually increasing plateau was reached during the 48-h injection as progressively longer residence-time flowpaths returned to the stream. Tailing behavior of the tracer after the injection ended was delayed between studies in a similar pattern to arrival time. This increased tailing suggests an increased influence of physical processes other than advection in the stream channel on the overall behavior of tracer in the study reach.

2.3. Electrical resistivity imaging

In this study we interpret electrical resistivity data and images originally presented by Ward et al. (2012a) using time series analysis; complete details of geophysical data collection and inversion can be found in that study. Briefly, electrical resistivity data were collected using a 10-channel Syscal Pro Resistivity Meter (IRIS Instruments, Orleans, France) at five transects perpendicular to the down-valley axis, each with 12 surface electrodes at 1–2 m spacing. Transects were co-located within piezometers previously installed by Wondzell (2006). ER data were collected using a mixed dipole–dipole array with a total sequence of 323 quadripoles per inverted data set, designed to provide reasonable resolution in the shallow subsurface in the valley bottom and allow increased
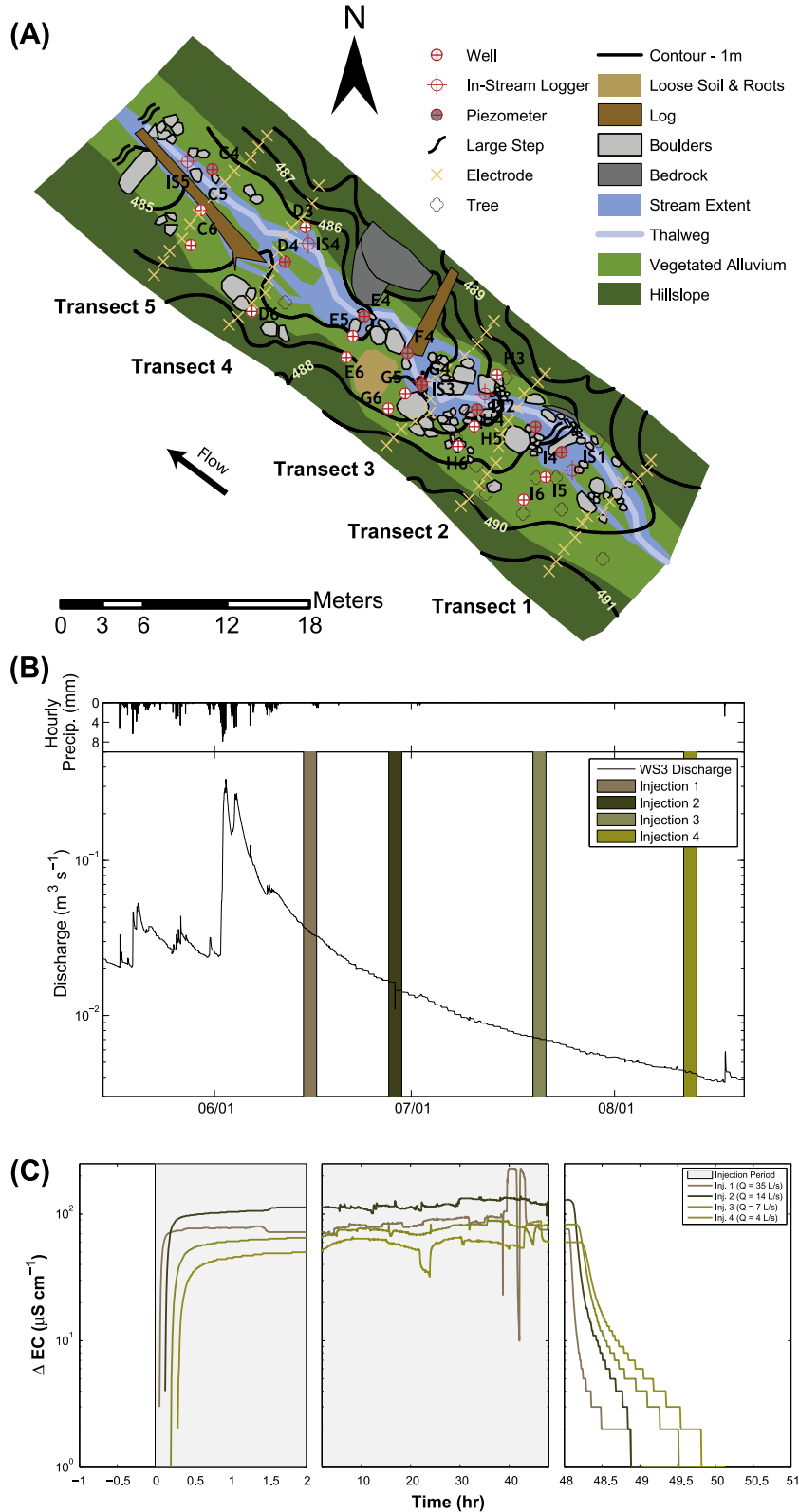
Fig. 1. (A) Site location and instrumentation maps for Watershed 3 in the H.J. Andrews Experimental Forest, located in the Cascade Range of central Oregon, USA. Piezometers and well transects are organized by letter (from C downstream to I upstream) and number (increasing from North to South across the valley); in-stream observations are identified by the prefix IS and location number. (Modified from Fig. 1B in Voltz et al. (2013)). Flow is from southeast to northwest. Solute tracers were injected into the stream approximately 50 m upstream of the study reach. (B) Watershed discharge and precipitation in the watershed during the 2010 study season. Flow was gauged at a weir located approximately 100 m downstream of each study reach. Injection periods for each solute tracer injection are shown as shaded bars. Dates on the X-axis are presented as MM/DD (reprinted from Fig. 2 in Ward et al. (2012a)). (C) Breakthrough curves at the upstream end of the study reach in the watershed, as the change in observed electrical conductivity (EC) of the surface water (a surrogate for the concentration of the sodium chloride tracer). Arrival time at the study reach was increasingly later as flow decreased during the season. Studies during lower flow conditions show increased tailing at late times, suggesting increased transient storage between the injection point and study reach (reprinted from Fig. 4 in Ward et al. (2012a)).

temporal resolution. Data collection applied by Ward et al. (2012a,b) includes quantification of stacking and reciprocal errors to ensure high-quality data were collected. Average stacking error (a measure of repeatability of electrical measurements) was 0.2% (range 0–50%) across all data considered in the study. Reciprocal data were collected for 55 of the 323 quadripoles, with average reciprocal error of 1.3% (range 0–100%) across all data considered in the study. ER data were inverted using the research code R2 (v2.6, Generalized 2-D Inversion of Resistivity Data, available at http://www.es.lancs.ac.uk/people/amb/Freeware/freeware.htm), implementing the difference inversion strategy of LaBrecque and Yang (2001) that seeks the change in model parameters from the starting model by inverting on the change in observed electrical data. The difference inversion scheme minimizes systematic errors in inversion models and reduces artifacts in the inversion images (LaBrecque and Yang, 2001). Each image collected during and after the tracer study was post-processed by calculating percent change from background (pre-tracer) for each inversion pixel. Notably, we did not account for the changing conductivity of the stream during the study; the stream represents a small proportion of the cross-section and its effect was considered negligible in the inversion (after Ward et al., 2010a,b, 2012a). Based on our estimates of stream cross-sectional area, the stream represents about 0.001–0.002% of the total inversion domain used for each transect and injection (for streams of 0.70 and 1.8 m^2, respectively). Under the highest discharge conditions, Ward et al. (2012a) report hyporheic areas ranging from 17 to 23 m^2; a 1.8 m^2 stream represents 7.8–10.6% of the total imaged target. For the lowest discharge conditions, Ward et al. (2012a) report hyporheic areas ranging from 14 to 34 m^2; a 0.70 m^2 stream represents 2.1–5.0% of the total imaged hyporheic zone. For comparison, Ward et al. (2010a,b) made this assumption for a stream cross-sectional area of 0.26 m^2 (estimated as 1.75-m by 0.15-m rectangular channel, from reported geometry of 1.5–2 m width and 0.1–0.2 m depth). In that study, the stream represented up to 52% of the imaged hyporheic area.

Pixels for analysis were limited to those where the diagonal of the resolution matrix was greater than or equal to 0.01 (i.e., 1% or more of a pixel's value is independent of adjacent pixels) and where solute was present to cause a minimum decrease of 3% in resistivity from background (using the chosen threshold as Ward et al. (2012a) for these data). The data analyzed in this study and threshold used to parse signal from noise are the same as applied in Ward et al. (2012a). We note here that the presence of solute inferred at the edges of the domain and depths could be either physical (e.g., transport through weathered bedrock) or an artifact of the inversion process. We emphasize here that results are sensitive to the thresholds chosen, as noted by Ward et al. (2010a,b, 2012a) and Menichino et al. (2012).

Ward et al. (2012a) demonstrate agreement in temporal trends between inversion pixel time series and observations of tracer presence in monitoring wells; electrical resistivity images provide distributed assessment of solute presence in the subsurface. Ward et al. (2012a) report that the peak cross-sectional size of the hyporheic zone during each injection was generally larger during high-flow conditions for upstream transects (T1–3), while extent was more consistent for downstream transects (T4–5). Ward et al. (2012a) present a detailed assessment of spatiotemporally variable trends in hyporheic extent as controlled by valley confinement and hydraulic gradients (both vertical and valley-bottom).

2.4. Time series analysis

In this study we analyze the time series of pixel resistivity in the inverted images. Hereafter the term "pixel resistivity" will be used to describe the predicted bulk resistivity value for individual pixels from inversion images, and "pixel time series" in reference to the time series of pixel resistivity values at one pixel from a series of inversion images. We calculated the first arrival of tracer at a pixel as the time at which the pixel first decreased by more than 3% of its pre-tracer value (again using the threshold of Ward et al. (2012a)). We calculated persistence as the time elapsed between the first- and last time at which the pixel value decreased by at least 3% of its pre-tracer value.

Temporal moments of time-variable data can be used to compress time series concentration histories into descriptive statistics (i.e., mean arrival time, variance, skewness). An nth order temporal moment (M_n) is calculated by:

$$M_n^{obs} = \int_0^\infty t^n r(t) dt \tag{1}$$

where t is time, and $r(t)$ is the normalized change in pixel resistivity. Field observations of resistivity, $R(t)$, are normalized as:

$$r(t) = \frac{R(t)}{\int_0^{+\infty} R(t) dt} \tag{2}$$

such that $M_0^{obs} = 1$ (i.e., the time integral of $r(t)$ is unity). The first temporal moment (i.e., $n = 1$) is interpreted as the mean arrival time of the breakthrough curve. Higher order temporal moments defined about the centroid (M_1^{obs}) can be calculated as:

$$\mu_2^{obs} = \int_0^\infty (t - M_1^{obs})^2 r(t) dt \tag{3}$$

and

$$\mu_3^{obs} = \int_0^\infty (t - M_1^{obs})^3 r(t) dt \tag{4}$$

where μ_2 (the second central moment) is the variance of the concentration profile, and μ_3 (the third central moment) is related to the skewness (Gupta and Cvetkovic, 2000; Harvey and Gorelick, 1995).

Next, to isolate the behavior of the system independently of the input signal, we calculate the temporal moments of the transfer function, $g(\tau)$, from the convolution integral for a system with linear behavior:

$$r(t) = \int_0^\infty g(\tau) r_{in}(t - \tau) d\tau \tag{5}$$

where r_{in} describe the time series of the input signal. Deconvolution is not necessary to obtain the temporal moments of the transfer function, provided that normalized moments are considered, as in our study. In this case, temporal moments of the transfer function can be calculated as:

$$M_n = M_n^{obs} - M_n^{r_{in}} \tag{6}$$

$$\mu_2 = \mu_2^{obs} - \mu_2^{r_{in}} \tag{7}$$

$$\mu_3 = \mu_3^{obs} - \mu_3^{r_{in}} \tag{8}$$

where $M_1^{r_{in}} = 24$ h, $\mu_2^{r_{in}} = 192$ h^2, $\mu_3^{r_{in}} = 0$ h^3 for the constant rate input. We omitted pixels where $M_1 < 0$ and/or $\mu_2 < 0$ from all time-series analyses (about 2% of all pixels; see Supplemental Fig. 1 for further details). These conditions indicate arrival before an input entered the stream and a net decrease in temporal variance, respectively, both of which are not physically possible. These adjustments isolate the system behavior independent of the input signal.

Finally, we calculated the dimensionless coefficient of variation, CV, as:

$$CV = \frac{\mu_2^{1/2}}{\mu_1}. \tag{9}$$

Skewness (γ, dimensionless) was calculated as:

$$\gamma = \frac{\mu_3}{\mu_2^{3/2}}. \tag{10}$$

The coefficient of variation, CV, provides a normalized metric of increases temporal variance in the observed timeseries. Constant CV values are indicative of convective scaling of the signal (i.e., the observed spread can be interpreted by differential advection and scales inversely with the mean velocity). The skewness, γ, describes the asymmetry of the distribution in time, with positive values suggesting time series that are more heavily tailed at late times. It is important to note that a combination of several physical processes produces each of the moments (i.e., some combination of advection, longitudinal dispersion, and diffusion between flowpaths or into less mobile locations); they cannot be physically parsed based on the solute signal observed. Throughout the manuscript, interpretation of temporal moments, coefficient of variation, and skewness are always with respect to the transfer function, as calculated in Eqs. 6–10. Temporal moment analyses, particularly those of higher-order moments, are sensitive to truncation of the time-series and to late-time noise in the signal. Finally, mean, median, and standard deviation values for time-series analysis at each transect were regressed against discharge for all metrics.

2.5. ANOVA for electrical resistivity image time-series

We used a one-way analysis of variance (ANOVA) to test for significant differences in first arrival, persistence, and temporal moments. This statistical test has several underlying assumptions, including that data are normally distributed, samples are independent, and variance of each data set is comparable. First, we applied ANOVA to test for significant differences between individual transects for each injection. Next, we applied ANOVA to test for significant differences for each individual transect under the four discharge conditions that were studied. As applied here, the resultant probability (p-value) describes the probability that at least one sample is drawn from a population with a mean value significantly different than the others. In this study, we consider $p < 0.001$ indicates at least one of the populations being considered is significantly different than the others.

3. Results

3.1. First arrival times

First arrival times were generally fastest near the stream and slower with increasing distance from the stream at all transects (Fig. 2). In lower reaches (T4–5), the rapid tracer arrival in the subsurface was over a much larger spatial area, compared to upstream reaches during all flow conditions. This arrival suggests rapid, extensive downwelling of stream water into the hyporheic zone at T4 and T5, both located in a gravel wedge in the valley bottom. Tracer arrival times in the stream at the study reach are less than 0.5 h (Fig. 1C). The timescale of advective transport in the stream does not change enough through the season to be the only factor leading to these differences.

Considering all transect-average values and discharge conditions, first arrival times decrease with increasing discharge (Fig. 3A, $r^2 = 0.08$). The mean, median, and standard deviation of first arrival time decrease with increasing discharge at T1, T2, T4, and T5, and increase with increasing discharge at T3 (Table 1). For trends in mean, median, and standard deviation with discharge reported above, r^2 ranges are 0.013–0.991, 0.013–0.863, and 0.132–0.617, respectively (Table 1). At transects 1 and 3, there is a larger proportion of pixels with later first arrival times for

injection 2, compared to other injections (see CDFs in Supplemental material).

Using a one-way ANOVA, we found significant differences between transects for first arrival times ($p \ll 0.001$; Table 1) for all discharge conditions. Additionally, we found significant differences in the distribution of first arrival times when considering each individual transect across the discharge conditions studied ($p \ll 0.001$; Table 1). Differences between transects and discharge conditions are visualized in notched box-plots in the Supplemental material; box plots with overlapping notched regions are not significantly different from one another. These analyses are provided for first arrival time, and for all subsequent metrics considered.

3.2. Persistence

Tracer persistence, is presented for all transects and injections in Fig. 4. Persistence generally increased with decreasing discharge at all locations (Fig. 3B, $r^2 = 0.15$). This overall trend is indicative of slower transport along subsurface flowpaths (and therefore a longer flowpath residence time) during lower-flow injections. The areas of lower persistence near the stream surrounded by higher-persistence pixels (e.g., the ~60-h persistence pixels surrounded by those with 80+ hour persistence in injection 2, T2 in Fig. 4) are indicative of an advection-dominated region where solute was rapidly flushed from flowpaths, surrounded by a domain that is in less rapid communication with the stream. We note here that the analysis was ended at 120 h after the injection started; some flowpaths may have longer persistence than the monitoring duration.

For temporal persistence, mean and median values decrease with increasing discharge for T1, T2, and T5, and increase with increasing discharge for T3 and T4. At all transects, the standard deviation of temporal persistence decreases with increasing discharge. For trends in mean, median, and standard deviation with discharge reported above, r^2 ranges are 0.133–0.844, 0.374–0.990, and 0.537–0.994, respectively (Table 1). Downstream transects (T4–5) have a larger proportion of high-persistence pixels compared to upstream transects (T1–3) (see CDFs in Supplemental materials).

Using a one-way ANOVA, we found significant differences between transects for persistence ($p \ll 0.001$; Table 1) for all discharge conditions. Additionally, we found significant differences in the distribution of persistence when considering each individual transect across the discharge conditions studied ($p \ll 0.001$; Table 1).

3.3. Mean arrival time

The mean arrival time, M_1, of solute at each pixel is presented in Fig. 5. The fastest flowpaths are in the shallow subsurface near the stream channel (timescales of less than 50 h in many locations), while longer advective timescales are observed farther from the stream. T3 has a shrinking zone dominated by highly advective flow centered near $X = 7$ m. At T4, rapid arrival of tracer was observed during higher flow conditions (injection 2); arrival time was later during lower flow injections. Considering all transect-average values and discharge conditions, mean arrival time decreased with increasing discharge (Fig. 3C, $r^2 = 0.09$). Mean arrival times are generally latest during injection 2 at T1–3 (see CDFs in Supplemental material).

For T1, T2, T4, and T5, mean and median values for mean arrival time decreased with increasing discharge. For T3, mean and median arrival time increased with increasing discharge. For all transects, standard deviation of mean arrival time increased with increasing discharge. For trends in mean, median, and standard deviation with discharge reported above, r^2 ranges are
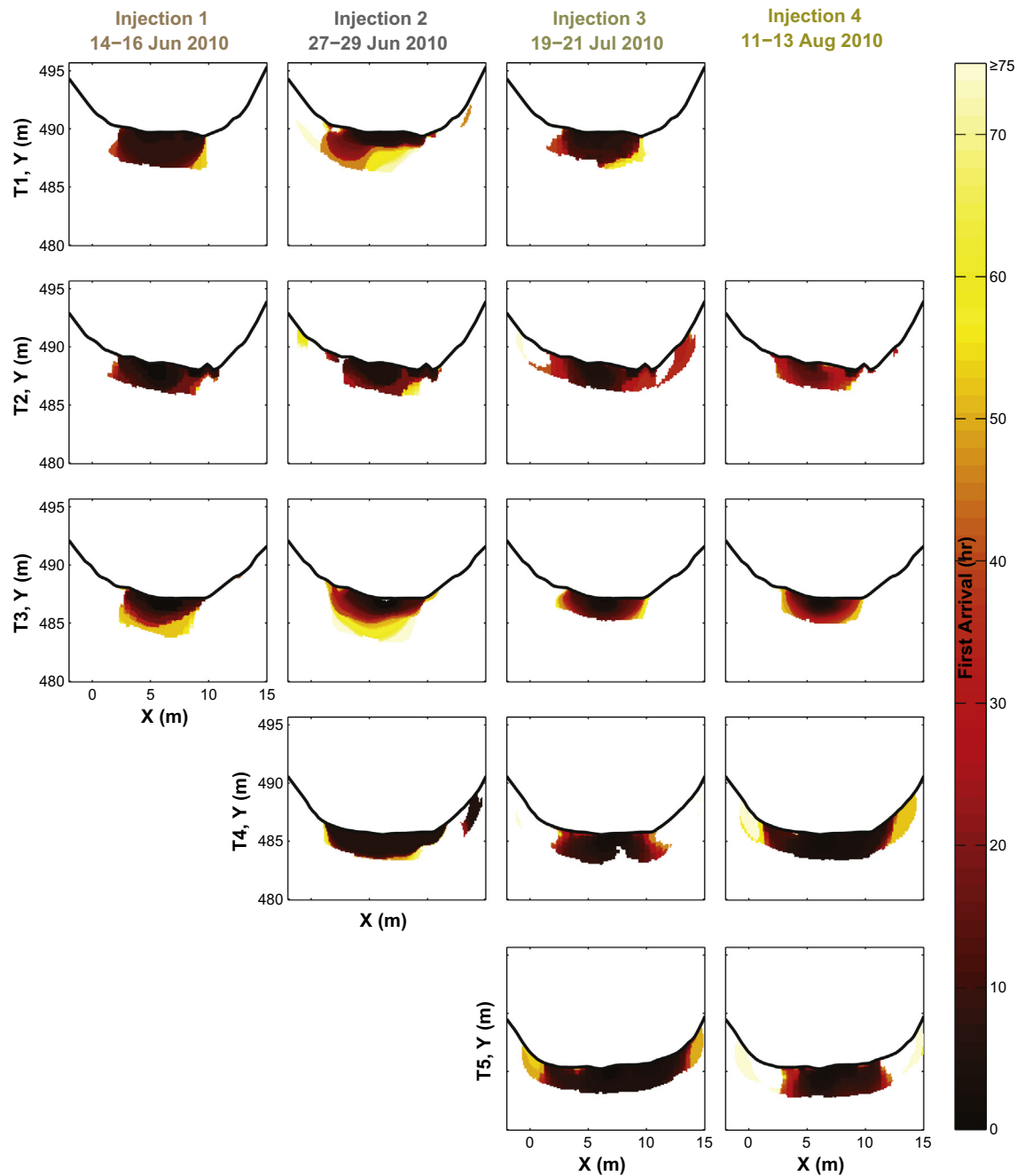
Fig. 2. Tracer first arrival time for all transects and injections for pixels where resolution above the set threshold. First arrival is defined here as the earliest time at which a decrease of 3% or more in pixel resistivity was observed. To restrict the analysis to only meaningful changes due to the solute tracer, pixels shown in each frame are those where there was high resolution in the inversion model, a change of at least −3% in resistivity was observed during the study, and the first and second temporal moments of the transfer function are physically meaningful.

0.006–0.838, 0.016–0.984, and 0.011–0.404, respectively (Table 1). Using a one-way ANOVA, we found significant differences between transects for mean arrival time ($p \ll 0.001$; Table 1) for all discharge conditions. Additionally, we found significant differences in the distribution of mean arrival times when considering each individual transect across the discharge conditions studied ($p \ll 0.001$; Table 1).

3.4. Temporal variance

Temporal variance of the solute pulse (μ_2) is generally lowest in locations nearest the stream channel, and increases with increasing distance from the channel (Fig. 6). In several transects, the low variance near the stream is surrounded by a "ring" of higher variance followed by lower variance (e.g., T3 during injection 2, Fig. 6). Ward et al. (2010a) report a similar pattern based on their numerical study, attributing the lower dispersion near the stream to an advection-dominated region of the subsurface. The low dispersion areas near the edges are interpreted as locations where tracer arrived more slowly, either allowing more time for transport processes other than advection to take place (convective scaling) or where the time-series was truncated. Considering all transect-average values and discharge conditions, temporal variance decreased with increasing discharge (Fig. 3D, $r^2 = 0.37$).

Mean and median values for temporal variance at T1 increase with increasing discharge; decreasing mean and median values
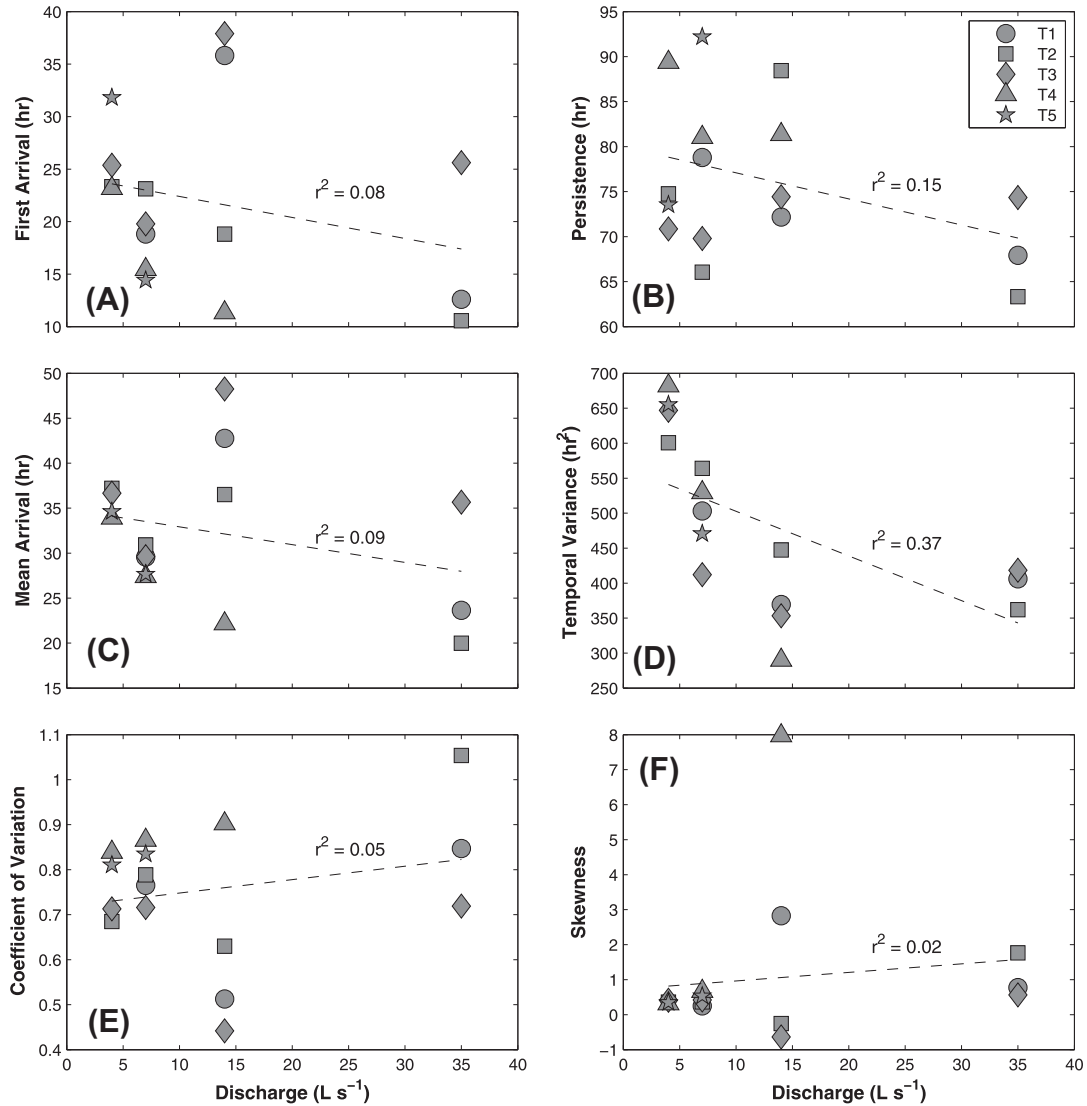
Fig. 3. Mean values of (A) first arrival time, (B) persistence, (C) mean arrival time, (D) temporal variance, (E) coefficient of variation, and (F) skewness as a function of stream discharge all transects and injections. Overall trends as the best-fit linear equation are shown as dashed lines, and r^2 is presented for each.

with increasing discharge were found at all other transects. The standard deviation of temporal variance increased with increasing discharge at all transects. For trends in mean, median, and standard deviation with discharge reported above, r^2 ranges are 0.195–0.990, 0.101–0.989, 0.062–0.821, respectively (Table 1). Using a one-way ANOVA, we found significant differences between transects for temporal variance ($p \ll 0.001$; Table 1) for all discharge conditions. Additionally, we found significant differences in the distribution of temporal variance when each individual transect across the discharge conditions studied ($p \ll 0.001$; Table 1).

3.5. Coefficient of variation

The CV is generally largest at locations near the stream channel (Fig. 7). Where the CV remains at the same value between injections, convective scaling can be inferred. For example, in T3, the area of rapid arrival and low temporal variance nearest the stream (visible as the red pixels in T3 located in near $X = 7$ m in Fig. 6, Injections 1–2, surrounded by a yellow area of higher temporal variance) has a CV that is variable between the discharge conditions, increasing with decreasing discharge. This patterns suggests convective scaling is not the only factor causing the spread of tracer in that location. In contrast, locations at that transect in the "ring" of

later arrival time surrounding the advection-dominated region are fairly consistent, suggesting increases in temporal variance and skewness can be explained by the change in advective timescales. Considering all transect-average values and discharge conditions, CV increased with increasing discharge (Fig. 3E, $r^2 = 0.05$).

Mean values for the coefficient of variation increased with increasing discharge for T1, T2, and T3, and decreased with increasing discharge for T4 and T5. Median values for CV increased with increasing discharge at all transects except T5. At all transects, the standard deviation of the CV increased with increasing discharge. For trends in mean, median, and standard deviation with discharge reported above, r^2 ranges are 0.004–0.980, 0.010–0.927, and 0.032–0.993, respectively (Table 1). Using a one-way ANOVA, we found significant differences between transects for coefficient of variation ($p \ll 0.001$; Table 1) for all discharge conditions. Additionally, we found significant differences in the distribution of the coefficient of variation when considering each individual transect across the discharge conditions studied ($p \ll 0.001$; Table 1).

3.6. Skewness

Skewness along individual subsurface flowpaths generally shows positive skewness near the stream channel, indicative of

Table 1

Statistical descriptions of the time-series metric for all transects and injections, slope and r^2 for best-fit trend lines of metrics vs. discharge, and one-way ANOVA results for differences between transects during each injection, and for differences between injections at each transect.

| Metric	Discharge (L s⁻¹)	T1 (Upstream)			T2			T3			T4			T5 (Downstream)			p[b]
		Mean	Med.	Std.	Mean	Med.	Std.	Mean	Med.	Std.	Mean	Med.	Std.	Mean	Med.	Std.	
First arrival (h)	35	12.61	7.99	12.27	10.56	8.20	10.57	25.62	16.41	21.03	–	–	–	–	–	–	<0.001
	14	35.82	29.14	26.79	18.81	12.77	19.77	37.90	38.32	26.09	11.33	5.51	14.78	–	–	–	<0.001
	7	18.81	10.96	18.42	23.12	21.17	19.49	19.79	13.39	16.55	15.45	9.81	15.97	14.42	5.16	17.70	<0.001
	4	–	–	–	23.33	21.22	10.52	25.38	21.43	17.23	23.16	5.96	27.73	31.82	8.83	38.53	<0.001
	m[c]	−0.425	−0.314	−0.328	−0.425	−0.429	−0.136	0.063	−0.090	0.124	−1.078	−0.147	−1.095	−5.798	−1.223	−6.943	–
	$r^{2,d}$	0.266	0.160	0.431	0.991	0.863	0.132	0.013	0.013	0.156	0.848	0.101	0.617	1[e]	1[e]	1[e]	–
	p[a]	<0.001			<0.001			<0.001			<0.001			<0.001			–
Persistance (h)	35	67.94	75.99	21.13	63.33	67.99	18.74	74.34	69.99	24.96	–	–	–	–	–	–	<0.001
	14	72.18	73.43	31.44	88.44	102.19	25.29	74.43	70.00	28.80	81.34	81.18	27.20	–	–	–	<0.001
	7	78.80	95.20	31.36	66.05	91.20	39.15	69.80	81.45	28.63	81.03	99.46	31.23	92.20	103.37	20.27	<0.001
	4	–	–	–	74.75	87.06	31.83	70.86	88.38	39.61	89.37	111.21	32.41	73.53	95.35	39.25	<0.001
	m[c]	−0.345	−0.500	−0.394	−0.295	−0.733	−0.536	0.127	−0.502	−0.332	−0.652	−2.934	−0.531	6.226	2.675	−6.327	–
	$r^{2,d}$	0.844	0.374	0.939	0.133	0.517	0.731	0.556	0.598	0.537	0.501	0.990	0.994	1[e]	1[e]	1[e]	–
	p[a]	<0.001			<0.001			<0.001			<0.001			<0.001			–
Mean arrival (h)	35	23.65	24.34	6.12	19.98	20.48	8.84	35.67	37.55	15.35	–	–	–	–	–	–	<0.001
	14	42.77	40.63	14.47	36.51	36.73	15.62	48.25	49.36	15.48	22.15	17.43	12.87	–	–	–	<0.001
	7	29.58	29.13	4.18	30.91	29.74	5.89	29.61	30.51	5.48	27.40	27.31	5.49	27.65	26.24	7.96	<0.001
	4	–	–	–	37.21	37.08	5.95	36.66	37.83	5.87	33.91	29.47	10.70	34.61	30.17	11.47	<0.001
	m[c]	−0.373	−0.310	−0.038	−0.501	−0.466	0.083	0.043	0.071	0.312	−1.100	−1.241	0.365	−2.322	−1.310	−1.170	–
	$r^{2,d}$	0.308	0.292	0.011	0.772	0.698	0.065	0.006	0.016	0.404	0.838	0.984	0.244	1[e]	1[e]	1[e]	–
	p[a]	<0.001			<0.001			<0.001			<0.001			<0.001			–
Temporal variance (h²)	35	406.25	437.75	144.22	362.09	403.92	136.79	418.39	459.57	147.54	–	–	–	–	–	–	<0.001
	14	369.36	421.68	184.15	447.28	529.03	206.74	353.36	404.26	201.22	289.91	273.91	147.69	–	–	–	<0.001
	7	503.14	483.11	69.41	564.02	495.44	137.24	412.04	408.18	34.02	529.41	524.20	61.67	470.65	467.14	63.82	<0.001
	4	–	–	–	600.70	603.69	81.19	647.08	630.96	86.84	682.09	687.78	74.67	654.98	665.84	111.24	<0.001
	m[c]	−2.256	−1.070	1.616	−7.381	−5.213	0.918	−4.095	−2.421	2.598	−38.331	−40.389	8.186	−61.443	−66.233	−15.806	–
	$r^{2,d}$	0.227	0.239	0.164	0.890	0.660	0.062	0.195	0.101	0.250	0.990	0.989	0.821	1[e]	1[e]	1[e]	–
	p[a]	<0.001			<0.001			<0.001			<0.001			<0.001			–
Coefficient of variation	35	0.85	0.75	0.09	1.05	1.13	0.32	0.72	0.33	0.39	–	–	–	–	–	–	<0.001
	14	0.51	0.59	0.26	0.63	0.24	0.22	0.44	−0.04	0.24	0.90	1.61	0.41	–	–	–	<0.001
	7	0.76	0.37	0.06	0.79	0.40	0.17	0.72	0.42	0.17	0.87	0.67	0.14	0.83	0.62	0.19	<0.001
	4	–	–	–	0.68	0.28	0.19	0.71	0.39	0.15	0.84	0.64	0.22	0.81	0.63	0.23	<0.001
	m[c]	0.006	0.012	−0.001	0.011	0.027	0.005	0.001	−0.002	0.008	0.006	0.104	0.022	0.008	−0.002	−0.014	–
	$r^{2,d}$	0.246	0.862	0.032	0.700	0.841	0.954	0.004	0.010	0.993	0.980	0.927	0.684	–	–	–	–
	p[a]	<0.001			<0.001			<0.001			<0.001			<0.001			–
Skewness	35	0.77	0.75	0.56	1.76	1.13	2.64	0.57	0.33	0.85	–	–	–	–	–	–	<0.001
	14	2.83	0.59	58.90	−0.25	0.24	5.27	−0.64	−0.04	18.97	7.97	1.61	132.76	–	–	–	<0.001
	7	0.25	0.37	0.50	0.36	0.40	0.34	0.42	0.42	0.37	0.67	0.67	0.36	0.53	0.62	0.57	<0.001
	4	–	–	–	0.36	0.28	0.38	0.41	0.39	0.28	0.31	0.64	0.79	0.35	0.63	0.76	<0.001
	m[c]	−0.008	0.012	−0.639	0.049	0.027	0.069	0.007	−0.002	−0.014	0.815	0.104	14.211	0.062	−0.002	−0.063	–
	$r^{2,d}$	0.008	0.862	0.076	0.641	0.841	0.173	0.030	0.010	0.000	0.936	0.927	0.913	1[e]	1[e]	1[e]	–
	p[a]	0.032			<0.001			<0.001			<0.001			<0.001			–

[a] Probability that behavior a transect is drawn from a population with the same mean across all four discharge conditions.
[b] Probability that behavior at all transects are drawn from populations with the same mean for a given discharge condition.
[c] Slope of best-fit linear regression for summary statistic vs. discharge.
[d] r^2 for the best-fit linear regression of summary statistic vs. discharge.
[e] Value is 1 because only two points were available for the regression.
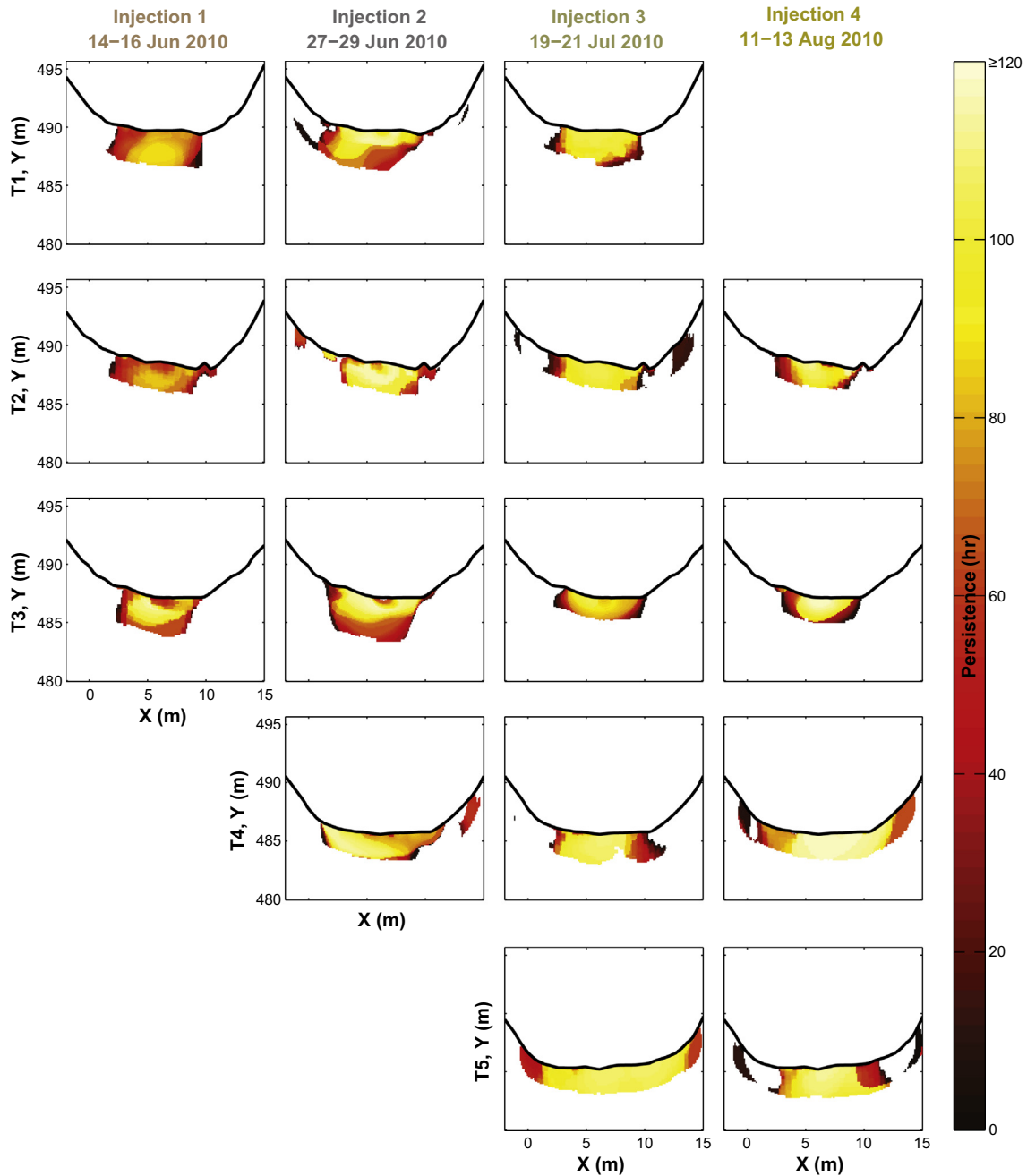
Fig. 4. Hyporheic persistence, defined here as the maximum range in times where a pixel decrease of 3% or more was observed, for each transect and injection. To restrict the analysis to only meaningful changes due to the solute tracer, pixels shown in each frame are those where there was high resolution in the inversion model, a change of at least −3% in resistivity was observed during the study, and the first and second temporal moments of the transfer function are physically meaningful.

late-time tailing commonly attributed to transport processes other than advection along a flowpath (Fig. 8). Skewness exhibits a similar spatial trend as temporal variance, with a "ring" of highly skewed breakthrough curves in the subsurface surrounding a region near the valley surface with near-zero skewness (for example, T3 during injection 2, Fig. 8). This pattern indicates advective transport dominated the "inside" of the ring, while processes other than advection had a larger influence on transport with increasing distance from the stream. Considering all transect-average values and discharge conditions, skewness increased with increasing discharge (Fig. 3F, $r^2 = 0.02$).

For T1, T2, T3, and T4, both mean and median skewness increased with increasing discharge; both decreased with increasing discharge at T5. For all transects, the standard deviation of skewness values increased with increasing discharge. For trends in mean, median, and standard deviation with discharge reported above, r^2 ranges are 0.008–0.936, 0.010–0.927, <0.001–0.913, respectively (Table 1). Using a one-way ANOVA, we found significant differences between transects for skewness ($p \ll 0.001$; Table 1) for all discharge conditions. Additionally, we found significant differences in the distribution of skewness values when considering each individual transect across the discharge conditions studied ($p \ll 0.001$; Table 1).
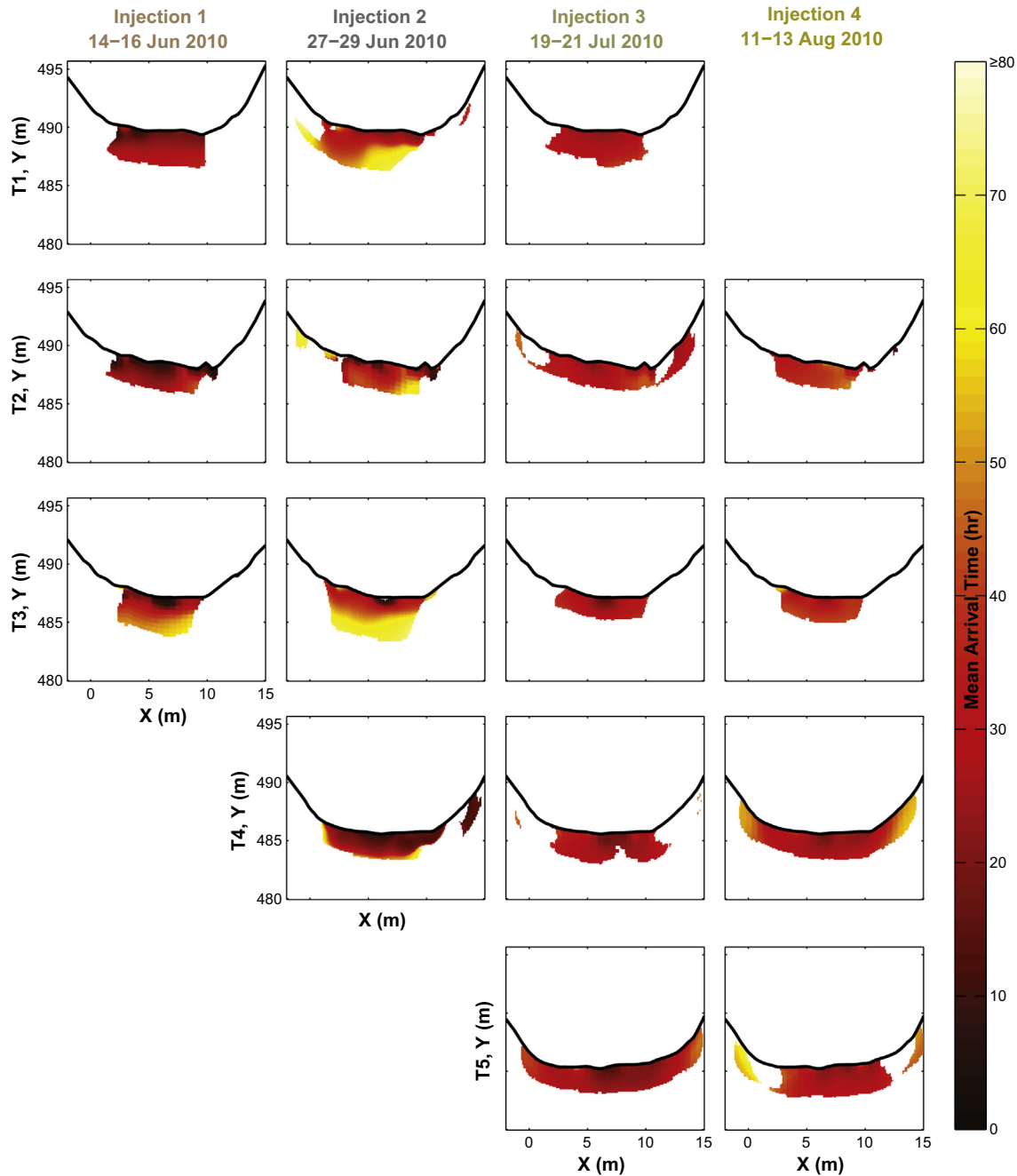
Fig. 5. Mean arrival time for each transect and injection. Advective timescales are generally fastest near the stream and during higher flow conditions. To restrict the analysis to only meaningful changes due to the solute tracer, pixels shown in each frame are those where there was high resolution in the inversion model, a change of at least −3% in resistivity was observed during the study, and the first and second temporal moments of the transfer function are physically meaningful.

4. Discussion

4.1. Heterogeneity and trends in hyporheic transport during baseflow recession

The results of this study demonstrate substantial variability in hyporheic transport processes, both as measured at individual transects and between transects. Furthermore, as seasonal baseflow recession occurs there are trends in transport behavior. As baseflow decreases, the solute tracer arrives more slowly both in the channel (due to slower advective velocities in the stream; Fig. 1C) and in the subsurface as seen in the ER inversions. Observed breakthrough curves for inversion pixels generally show

increased temporal variance and skewness throughout the season. The shrinking areas of advection-dominated transport in the subsurface near the stream (i.e., the locations with rapid first arrival and small skewness) suggest that changing hydraulic gradients around the channel and catchment wetness control subsurface transport (e.g., lateral groundwater gradients beyond the valley floor). The increasing standard deviation for all temporal moments and dimensionless metrics shows increased heterogeneity of hyporheic flowpaths during lower discharge conditions.

Transects in our study reach were located in contrasting morphology, with T1–2 in a bedrock confined location with an alluvial deposit, T3 near a bedrock pinch-point with little alluvial deposit, and T4–5 located in a gravel wedge. For first arrival time,
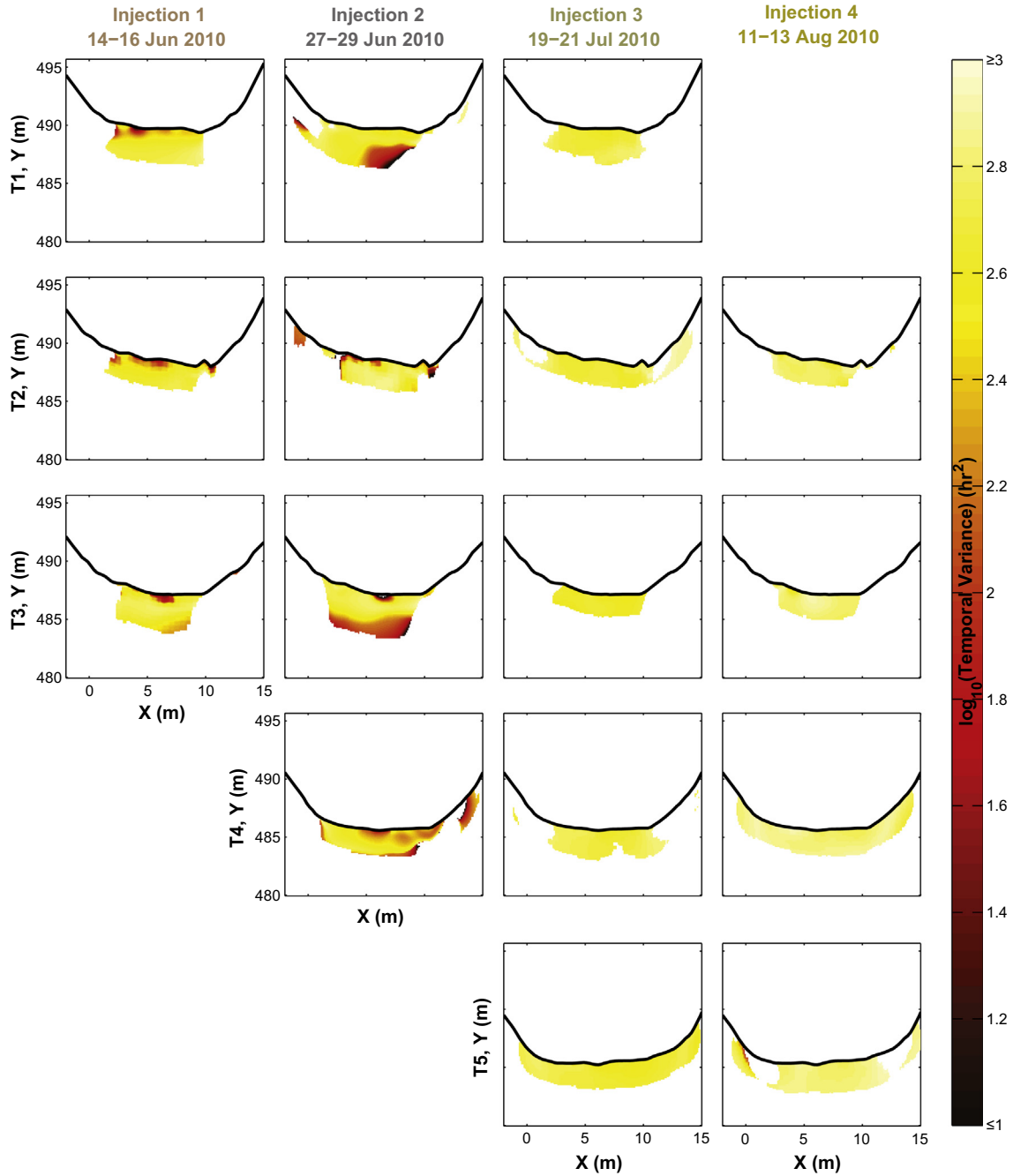
Fig. 6. Temporal variance for each transect and injection. Temporal variance is generally low adjacent to the stream, interpreted as an advection-dominated region of the subsurface, and in the boundaries of each cross-section. To restrict the analysis to only meaningful changes due to the solute tracer, pixels shown in each frame are those where there was high resolution in the inversion model, a change of at least -3% in resistivity was observed during the study, and the first and second temporal moments of the transfer function are physically meaningful.

persistence, and mean arrival time, mean and median values increased with discharge at T3, and decreased with discharge at T1–2 and T4–5. Mean first arrival time was faster at the downstream gravel wedge (T4–5) than at the alluvial deposit (T1–3) during injections 2 and 3. Mean coefficient of variation decreased with discharge at T4–5, and increased with discharge at T1–3; mean and median skewness decreased with increasing discharge at T5, and increased with discharge at all other locations. T3 is interpreted here as a geomorphologic transition from the pool-riffle structures upstream (T1–2) to the gravel wedge downstream (T4–5). The results above suggest these geomorphologic units

contrast in their response to baseflow recession, and in the transport of stream water along hyporheic flowpaths.

We emphasize here that the interpretation of these results must be in the context of two primary limitations. First, most trends with discharge have low r^2 values. We attribute this spread, at least in part, to the limited number of data points being analyzed. Secondly, results must be interpreted in the context of known limitations of electrical resistivity imaging. Out-of-plane effects could have caused tracer to be detected early than its actual arrival; results may be biased toward earlier first arrival. These effects could also cause detection later than its actual flushing from
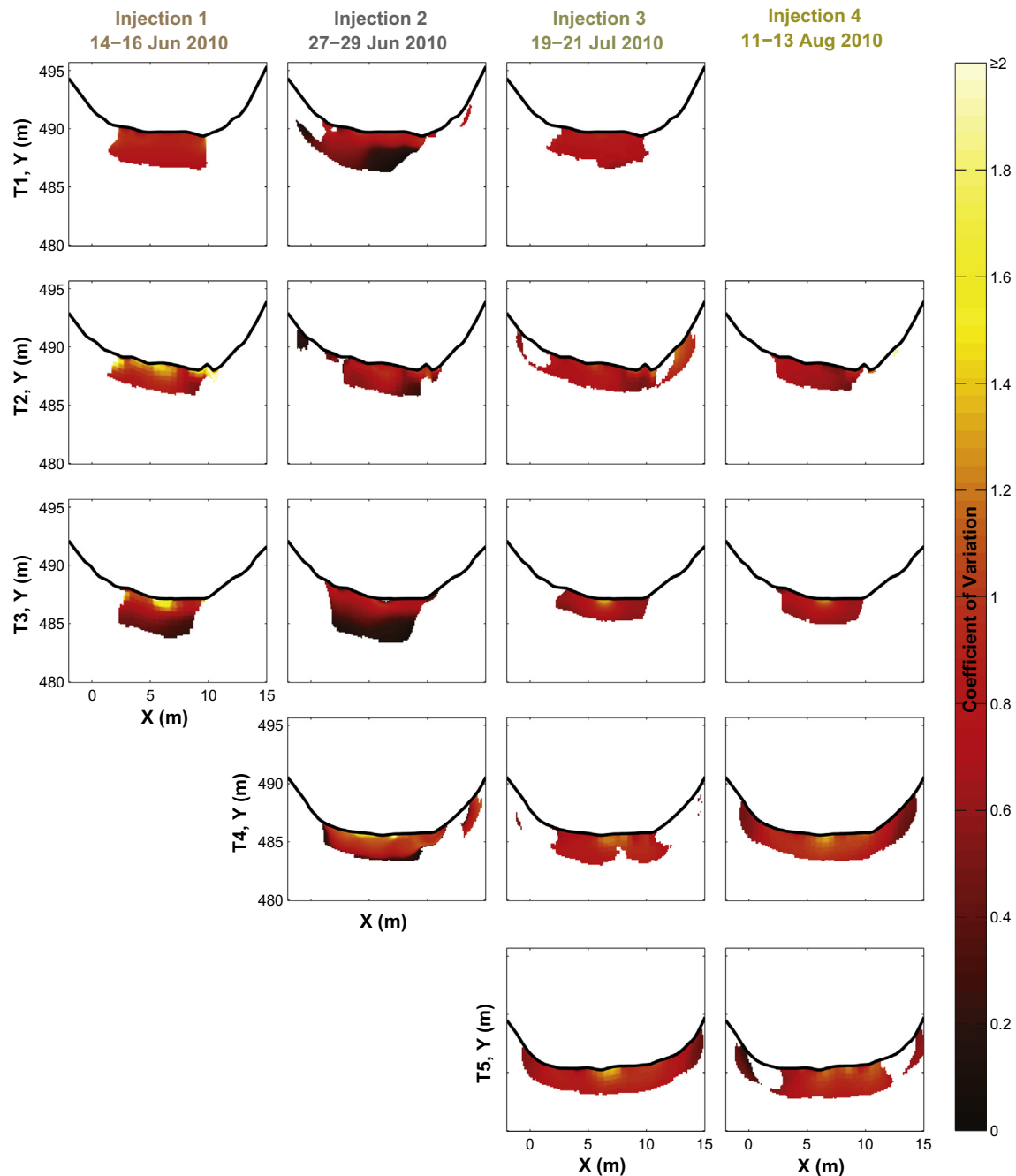
Fig. 7. Coefficient of variation for each transect and injection. To restrict the analysis to only meaningful changes due to the solute tracer, pixels shown in each frame are those where there was high resolution in the inversion model, a change of at least −3% in resistivity was observed during the study, and the first and second temporal moments of the transfer function are physically meaningful.

the transect, which would bias results toward longer persistence. This increased temporal variance in the input signal may have consequences for some interpreted metrics of transport (i.e., temporal variance, skewness), and could bias the interpreted mean arrival time if the error is not equal on the rising and falling limbs of the time-series. The inverse problem that must be solved to generate the images from field data is both ill-posed (i.e., non-unique solutions exist) and ill-conditioned (i.e., large model error may arise from small data errors) (Koestel et al., 2009), generating images that are oversmoothed and non-unique. The difference inversion scheme here is designed to minimize error between timesteps, but is not a perfect solution. We further acknowledge that changing the minimum resolution or minimum percent

change thresholds applied here and by Ward et al. (2012a) would define a different set of pixels for analysis.

4.2. Comparison of observations with common numerical models of stream–hyporheic interactions

Results of this study demonstrate a highly heterogeneous hyporheic zone, both at each inverted transect and at different geomorphologic features. Furthermore, the distribution of transport metrics is variable during baseflow recession. We found that the hyporheic zone is not well mixed, the hyporheic extent varies through time, and substantial down-valley transport in the subsurface can be inferred between transects (e.g., T4–5). In contrast,
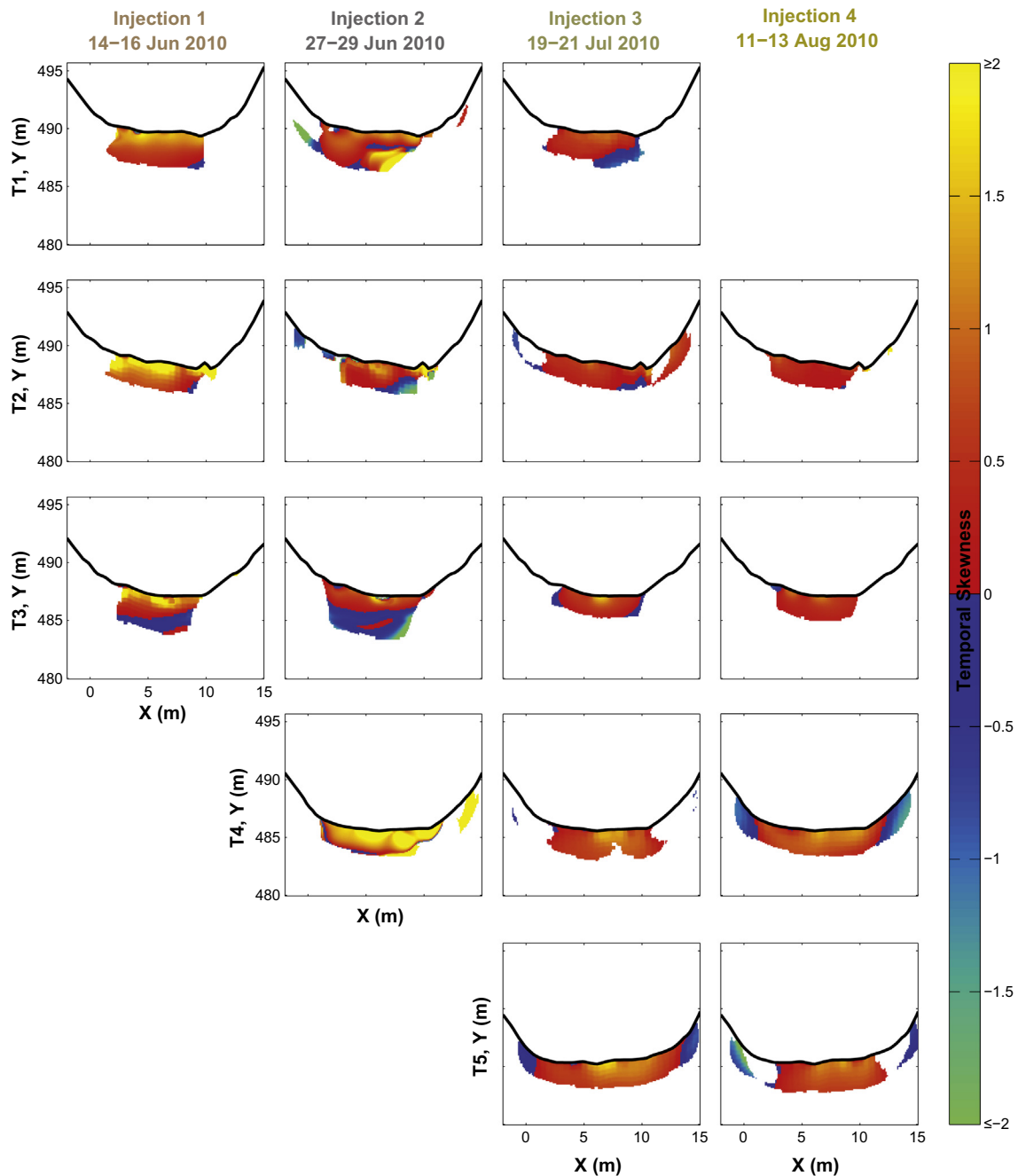
Fig. 8. Skewness for each transect and injection. To restrict the analysis to only meaningful changes due to the solute tracer, pixels shown in each frame are those where there was high resolution in the inversion model, a change of at least −3% in resistivity was observed during the study, and the first and second temporal moments of the transfer function are physically meaningful.

common stream solute transport model based on the transient storage equations of Bencala and Walters (1983) assume both an exponential distributions of solute residence times in transient storage at each spatial step and a well-mixed transient storage domain and no down-valley subsurface transport (e.g., Bencala and Walters, 1983; Haggerty et al., 2000, 2002; Thackston and Schnelle, 1970). While these numerical models have been demonstrated to fit field observations in the stream channel, they are known to be sensitive to only the shortest spatial and temporal flowpaths (commonly called the "window of detection" problem; Harvey et al., 1996; Harvey and Wagner, 2000). Much of the short transient storage commonly interpreted from such analyses can be attributed to in-channel dead zones (e.g., recirculating eddies

behind in-channel features; Choi et al., 2000; Gooseff et al., 2005, 2008; Thackston and Schnelle, 1970), or to very short residence time flowpaths in the subsurface. Observations using ER allow for a spatially distributed assessment of transport behavior, providing orders of magnitude more time-series, albeit as "soft data" subject to the limitations of ER, than monitoring in the stream channel or in a piezometer network. The repeated solute tracer experiments show a high degree of variability in transport processes through both time and space.

Based on the changing spatial distributions of each metric analyzed here and the CDFs (see Supplemental materials), the hyporheic zone is also dynamic in response to hydrological drivers. The distribution of first-arrival times, for example, can be interpreted

as a surrogate for the transit time distribution from the injection location to where the ER is sensitive to the tracer, which may be outside of the actual transect (e.g., Nimmer et al., 2008). While the integration of assumed distributions (i.e., exponential, power law) may provide adequate fits for reach-scale in-stream breakthrough curves, the behavior of individual flowpaths at a given location is much more complicated.

5. Conclusions

Our ability to collect high-resolution data in repeated studies during baseflow recession allowed us to characterize spatial variability in solute transport and their dynamics in response to changing baseflow conditions. This study is the first, to the best of our knowledge, to analyze the distribution of hyporheic zone transport processes based on ER images monitoring these processes in situ. Temporal moment analysis of ER images provides a spatially distributed characterization of solute transport in the hyporheic zone. Analysis of this data set allows for assessment of spatial patterns in transport along a stream reach, and hyporheic transport patterns (e.g., spatial distributions of temporal moment analysis, first arrival times, and hyporheic persistence). This distributed transport process information could be used to improve existing groundwater flow models. Indeed, numerical experiments demonstrate the potential to derive hydraulic conductivity fields from ER inversions and constrain model formulations for subsurface architecture (Pollock and Cirpka, 2010; Ward et al., 2012a).

Overall, this study demonstrates: (1) the variability in hyporheic transport processes increases with decreasing baseflow, as evidenced by increasing standard deviations for mean arrival time, temporal variance, coefficient of variation, and skewness in time-series ER images; (2) all metrics of transport are significantly different between transects during each replicate study, suggesting high degrees of heterogeneity in a relatively small study reach; (3) all metrics of transport are significantly different between discharge conditions at an individual transects, suggesting discharge exerts a primary control on hyporheic transport; and (4) geomorphologic units are a control on rates and variability of transport along hyporheic flowpaths.

Acknowledgments

Appendix A. Supplementary material

Supplementary data associated with this article can be found, in the online version, at http://dx.doi.org/10.1016/j.jhydrol.2014.05.036.

References

Argerich, A., Haggerty, R., Marti, E., Sabater, F., Zarnetske, J., 2011. Quantification of metabolically active transient storage (MATS) in two reaches with contrasting transient storage and ecosystem respiration. J. Geophys. Res. 116, G03034.

Battin, T.J., 1999. Hydrologic flow paths control dissolved organic carbon fluxes and metabolism in an alpine stream hyporheic zone. Water Resour. Res. 35 (10), 3159–3169.

Battin, T.J., 2000. Hydrodynamics is a major determinant of streambed biofilm activity: from the sediment to the reach scale. Limnol. Oceanogr. 45 (6), 1308–1319.

Bencala, K.E., Walters, R.A., 1983. Simulation of solute transport in a mountain pool-and-riffle stream: a transient storage model. Water Resour. Res. 19 (3), 718–724.

Beven, K.J., 1993. Prophecy, reality and uncertainty in distributed hydrological modelling. Adv. Water Resour. 16 (1), 41–51.

Beven, K.J., 2006. A manifesto for the equifinality thesis. J. Hydrol. 320 (1–2), 18–36.

Binley, A.M., Henry-Poulter, S., Shaw, B., 1996. Examination of solute transport in an undisturbed soil column using electrical resistance tomography. Water Resour. Res. 32 (4), 763–769.

Binley, A.M., Cassiani, G., Deiana, R., 2010. Hydrogeophysics: opportunities and challenges. Boll. Geofisica Teorica Appl. 51 (4), 267–284.

Boano, F., Revelli, R., Ridolfi, L., 2008. Reduction of the hyporheic zone volume due to the stream-aquifer interaction. Geophys. Res. Lett. 35 (9), L09401.

Boano, F., Camporeale, C., Revelli, R., 2010. A linear model for the coupled surface-subsurface flow in a meandering stream. Water Resour. Res. 46 (7), W07535.

Boulton, A.J., Datry, T., Kasahara, T., Mutz, M., Stanford, J.A., 2010. Ecology and management of the hyporheic zone: stream-groundwater interactions of running waters and their floodplains. J. N. Am. Benthol. Soc. 29 (1), 26–40.

Bredehoeft, J.D., Konikow, L.F., 1993. Ground water models: validate or invalidate. Ground Water 31 (2), 178–179.

Brunke, M., Gonser, T., 1997. The ecological significance of exchange processes between rivers and groundwater. Freshw. Biol. 37, 1–33.

Cardenas, M.B., Markowski, M.S., 2011. Geoelectrical imaging of hyporheic exchange and mixing of river water and groundwater in a large regulated river. Environ. Sci. Technol. 45 (4), 1407–1411. http://dx.doi.org/10.1021/es103438a.

Cardenas, M.B., Wilson, J.L., 2007. Exchange across a sediment–water interface with ambient groundwater discharge. J. Hydrol. 346 (3–4), 69–80.

Choi, J., Harvey, J.W., Conklin, M.H., 2000. Characterizing multiple timescales of stream and storage zone interaction that affect solute fate and transport in streams. Water Resour. Res. 36 (6), 1511–1518.

Cirpka, O.A., Kitanidis, P.K., 2000. Characterization of mixing and dilution in heterogeneous aquifers by means of local temporal moments. Water Resour. Res. 36 (5), 1221–1236.

Day-Lewis, F.D., Singha, K., 2008. Geoelectrical inference of mass transfer parameters using temporal moments. Water Resour. Res. 44 (5), W05201.

Day-Lewis, F.D., Singha, K., Binley, A.M., 2005. Applying petrophysical models to radar travel time and electrical resistivity tomograms: resolution-dependent limitations. J. Geophys. Res. 110 (B8), B08206.

Day-Lewis, F.D., Chen, Y., Singha, K., 2007. Moment inference from tomograms. Geophys. Res. Lett. 34 (22), L22404.

Doetsch, J., Linde, N., Vogt, T., Binley, A.M., Green, A.G., 2012. Imaging and quantifying salt-tracer transport in a riparian groundwater system by means of 3D ERT monitoring. Geophysics 77 (5), B207–B218.

Dyrness, C.T., 1969. Hydrologic properties of soils on three small watersheds in the western Cascades of Oregon. USDA FOREST SERV RES NOTE PNW-111, SEP 1969. 17 p.

Gooseff, M.N., McGlynn, B.L., 2005. A stream tracer technique employing ionic tracers and specific conductance data applied to the Maimai catchment, New Zealand. Hydrol. Process. 19 (13), 2491–2506.

Gooseff, M.N., LaNier, J., Haggerty, R., Kokkeler, K., 2005. Determining in-channel (dead zone) transient storage by comparing solute transport in a bedrock channelñalluvial channel sequence, Oregon. Water Resour. Res. 41 (6), W06014.

Gooseff, M.N., Payn, R.A., Zarnetske, J.P., Bowden, W.B., McNamara, J.P., Bradford, J.H., 2008. Comparison of in-channel mobile-immobile zone exchange during instantaneous and constant rate stream tracer additions: implications for design and interpretation of non-conservative tracer experiments. J. Hydrol. 357 (1–2), 112–124.

Gupta, A., Cvetkovic, V., 2000. Temporal moment analysis of tracer discharge in streams: combined effect of physicochemical mass transfer and morphology. Water Resour. Res. 36 (10).

Haggerty, R., McKenna, S.A., Meigs, L.C., 2000. On the late-time behavior of tracer test breakthrough curves. Water Resour. Res. 36 (12).

Haggerty, R., Wondzell, S.M., Johnson, M.A., 2002. Power-law residence time distribution in the hyporheic zone of a 2nd-order mountain stream. Geophys. Res. Lett. 29 (13), 18.1–18.4.

Harvey, J.W., Bencala, K.E., 1993. The effect of streambed topography on surface-subsurface water exchange in mountain catchments. Water Resour. Res. 29 (1), 89–98.

Harvey, C.F., Gorelick, S.M., 1995. Temporal moment-generating equations: modeling transport and mass transfer in heterogeneous aquifers. Water Resour. Res. 31 (8).

Harvey, J.W., Wagner, B.J., 2000. Quantifying hydrologic interactions between streams and their subsurface hyporheic zones. In: Jones, J.B., Mulholland, P.J. (Eds.), Streams and Ground Waters. Academic Press, San Diego, CA, USA, pp. 3–44.

Harvey, J.W., Wagner, B.J., Bencala, K.E., 1996. Evaluating the reliability of the stream tracer approach to characterize stream-subsurface water exchange. Water Resour. Res. 32 (8), 2441–2451.

Hassan, A.E., 2004. Validation of numerical ground water models used to guide decision making. Ground Water 42 (2), 277–290.

Jardani, A., Revil, A., Dupont, J.P., 2013. Stochastic joint inversion of hydrogeophysical data for salt tracer test monitoring and hydraulic conductivity imaging. Adv. Water Resour. 52, 62–77.

Kasahara, T., Wondzell, S.M., 2003. Geomorphic controls on hyporheic exchange flow in mountain streams. Water Resour. Res. 39 (1), SBH 3-1–SBH 3-14.

Kemna, A., Kulessa, B., Vereecken, H., 2002. Imaging and characterisation of subsurface solute transport using electrical resistivity tomography (ERT) and equivalent transport models. J. Hydrol. 267 (3–4), 125–146.

Koch, K., Wenninger, J., Uhlenbrook, S., Bonell, M., 2009. Joint interpretation of hydrological and geophysical data: electrical resistivity tomography results from a process hydrological research site in the Black Forest Mountains, Germany. Hydrol. Proc. 23 (10), 1501–1513.

Koestel, J., Vanderborght, J., Javaux, M., Kemna, A., Binley, A.M., Vereecken, H., 2009. Noninvasive 3-D transport characterization in a sandy soil using ERT: 1. Investigating the validity of ERT-derived transport parameters. Vadose Zone J. 8 (3), 711–722.

Konikow, L.F., Bredehoeft, J.D., 1992. Ground-water models cannot be validated. Adv. Water Resour. 15 (1), 75–83.

Krause, S., Hannah, D.M., Fleckenstein, J.H., Heppell, C.M., Kaeser, D., Pickup, R., Pinay, G., Robertson, A.L., Wood, P.J., 2011. Inter-disciplinary perspectives on processes in the hyporheic zone. Ecohydrology 4 (4), 481–499.

LaBrecque, D.J., Yang, X., 2001. Difference inversion of ERT data: a fast inversion method for 3-D in situ monitoring. J. Environ. Eng. Geophys. 6.

Menichino, G.T., Ward, A.S., Hester, E.T., 2012. Macropores as preferential flow paths in meander bends. Hydrol. Process.

Nimmer, R.E., Osiensky, J.L., Binley, A.M., Williams, B.C., 2008. Three-dimensional effects causing artifacts in two-dimensional, cross-borehole, electrical imaging. J. Hydrol. 359, 59–70.

Oreskes, N., Shrader-Frechette, K., Belitz, K., 1994. Verification, validation, and confirmation of numerical models in the earth sciences. Science, 263.

Payn, R.A., Gooseff, M.N., McGlynn, B., Bencala, K.E., Wondzell, S.M., 2009. Channel water balance and exchange with subsurface flow along a mountain headwater stream in Montana, United States. Water Resour. Res., 45.

Pidlisecky, A., Singha, K., Day-Lewis, F.D., 2011. A distribution-based parametrization for improved tomographic imaging of solute plumes. Geophys. J. Int. 187 (1), 214–224.

Poeter, E., 2007. All models are wrong, how do we know which are useful? Ground Water 45 (4), 390–391.

Pollock, D., Cirpka, O.A., 2008. Temporal moments in geoelectrical monitoring of salt-tracer experiments. Water Resour. Res. 44 (12), W12416. http://dx.doi.org/10.1029/2008WR007014.

Pollock, D., Cirpka, O.A., 2010. Fully coupled hydrogeophysical inversion of synthetic salt tracer experiments. Water Resour. Res. 46 (7), W07501.

Pollock, D., Cirpka, O.A., 2012. Fully coupled hydrogeophysical inversion of a laboratory salt tracer experiment monitored by Electrical Resistivity Tomography. Water Resour. Res. 48 (1), W01505. http://dx.doi.org/10.1029/2011WR010779.

Schmid, B.H., 2003. Temporal moments routing in streams and rivers with transient storage. Adv. Water Resour. 26 (9), 1021–1027.

Singha, K., Gorelick, S.M., 2005. Saline tracer visualized with three-dimensional electrical resistivity tomography: field-scale spatial moment analysis. Water Resour. Res. 41 (5), W05023.

Singha, K., Gorelick, S.M., 2006. Effects of spatially variable resolution on field-scale estimates of tracer concentration from electrical inversions using Archieís law. Geophysics 71, G83.

Singha, K., Day-Lewis, Frederick D., Lane, J.W., 2007. Geoelectrical evidence of bicontinuum transport in groundwater. Geophys. Res. Lett. 34 (12), 12401.

Singha, K., Pidlisecky, A., Day-Lewis, F.D., Gooseff, M.N., 2008. Electrical characterization of non-Fickian transport in groundwater and hyporheic systems. Water Resour. Res. 44 (3).

Slater, L., Binley, A.M., Daily, W., Johnson, R., 2000. Cross-hole electrical imaging of a controlled saline tracer injection. J. Appl. Geophys. 44 (2–3), 85–102.

Slater, L., Binley, A.M., Versteeg, R., Cassiani, G., Birken, R., Sandberg, S., 2002. A 3D ERT study of solute transport in a large experimental tank. J. Appl. Geophys. 49 (4), 211–229.

Storey, R.G., Howard, K.W.F., Williams, D.D., 2003. Factors controlling riffle-scale hyporheic exchange flows and their seasonal changes in a gaining stream: a three-dimensional groundwater flow model. Water Resour. Res. 39 (2), 1034.

Thackston, E.L., Schnelle, K.B.J., 1970. Predicting effects of dead zones on stream mixing. J. Sanit. Eng. Div. 96 (2), 319–331.

Toran, L., Nyquist, J.E., Fang, A.C., Ryan, R.J., Rosenberry, D.O., 2012. Observing lingering hyporheic storage using electrical resistivity: variations around stream restoration structures, Crabby Creek, PA. Hydrol. Process. 27, 1411–1425.

Voltz, T.J., 2011. Riparian hydraulic gradient and water table dynamics in two steep headwater streams, M.S. Thesis, Pennsylvania State Univ., University Park, PA, 167 pp.

Voltz, T., Gooseff, M., Ward, A.S., Singha, K., Fitzgerald, M., Wagener, T., 2013. Riparian hydraulic gradient and stream-groundwater exchange dynamics in steep headwater valleys. J. Geophys. Res. Earth Surf. 118, 953–969. http://dx.doi.org/10.1002/jgrf.20074.

Ward, A.S., Gooseff, M.N., Singha, K., 2010a. Characterizing hyporheic transport processes – interpretation of electrical geophysical data in coupled stream–hyporheic zone systems during solute tracer studies. Adv. Water Resour. 33, 1320–1330.

Ward, A.S., Gooseff, M.N., Singha, K., 2010b. Imaging hyporheic zone solute transport using electrical resistivity. Hydrol. Process. 24 (7), 948–953.

Ward, A.S., Fitzgerald, M., Gooseff, M.N., Voltz, T.J., Binley, A.M., Singha, K., 2012a. Correction to "Hydrologic and geomorphic controls on hyporheic exchange during baseflow recession in a headwater mountain stream". Water Resour. Res. 48 (8), W08903.

Ward, A.S., Fitzgerald, M., Gooseff, M.N., Voltz, T.J., Binley, A.M., Singha, K., 2012b. Hydrologic and geomorphic controls on hyporheic exchange during base flow recession in a headwater mountain stream. Water Resour. Res. 48 (4), W04513.

Ward, A.S., Payn, R.A., Gooseff, M.N., McGlynn, B.L., Bencala, K.E., Kelleher, C.A., Wondzell, S.M., Wagener, T., 2013a. Variations in surface water–ground water interactions along a headwater mountain stream: Comparisons between transient storage and water balance analyses. Water Resour. Res., In Press.

Ward, A.S., Gooseff, M.N., Singha, K., 2013b. How does subsurface characterization affect simulations of hyporheic exchange? Ground Water 51 (1), 14–28.

Williams, D.D., 1993. Nutrient and flow vector dynamics at the hyporheic/groundwater interface and their effects on the interstitial fauna. Hydrobiologia 251 (1), 185–198.

Wondzell, S.M., 2006. Effect of morphology and discharge on hyporheic exchange flows in two small streams in the Cascade Mountains of Oregon, USA. Hydrol. Process. 20 (2), 267–287.

Wondzell, S.M., Swanson, F.J., 1996. Seasonal and storm dynamics of the hyporheic zone of a 4th-order mountain stream. 1: hydrologic processes. J. N. Am. Benthol. Soc. 15 (1), 3–19.

Wondzell, S.M., LaNier, J., Haggerty, R., 2009. Evaluation of alternative groundwater flow models for simulating hyporheic exchange in a small mountain stream. J. Hydrol. 364 (1–2), 142–151.

Wroblicky, G.J., Campana, M.E., Valett, H.M., Dahm, C.N., 1998. Seasonal variation in surface-subsurface water exchange and lateral hyporheic area of two stream-aquifer systems. Water Resour. Res. 34 (3), 317–328.

Zarnetske, J.P., Haggerty, R., Wondzell, S.M., Baker, M.A., 2011. Dynamics of nitrate production and removal as a function of residence time in the hyporheic zone. J. Geophys. Res. 116 (G1), G01025.